APPENDIX B

Publication P8

Repo A.-K., Rasilo P., Arkkio A. Dynamic electromagnetic torque model and parameter estimation for a deep-bar induction machine. *IET Electric Power Applications*, in press.

Dynamic electromagnetic torque model and parameter estimation for a deep-bar induction machine

Anna-Kaisa Repo, Paavo Rasilo, and Antero Arkkio
Helsinki University of Technology
Laboratory of Electromechanics
P.O. Box 3000, FI-02015 TKK, Finland

Acknowlegdement

Dr. Seppo Aatola from VTT Technical Research Centre of Finland provided the know-how and equipment for the torsional oscillation measurements. The research has been supported by The Graduate School in Electrical Engineering and TEKES (Finnish Funding Agency for Technology and Innovation).

Abstract — A dynamic analytical electromagnetic torque model for a deep-bar induction machine is presented. The model is based on the space-vector theory of electrical machines. The parameters are estimated using the data provided by the numerical impulse response test performed within the two-dimensional time-stepping finite element analysis (FEA). Two different impulse tests are studied. The impulse excitation is applied to the stator voltage and rotor position angle, and the parameter estimates are compared. The applicability of the impulse test is based on the assumption of linear behaviour in the neighbourhood of an operation point. Hence, one of the main objectives is to study the validity of the impulse test. From the results of the angle impulse test, a frequency range of negative damping is detected. The phenomenon is also studied by measurements.

1 Introduction

The motivation for the work is adopted from the studies performed within torsional oscillations of electrical machines [1], [2]. The stability analysis of induction machines has been discussed mainly in the 50's, for example in [3]. The majority of studies have focused on detecting, modelling and control of torsional oscillations in synchronous machines [4]. Recently, an analytical model suitable for predicting torsional oscillations of both synchronous and induction machines has been presented [5] but not applied to induction machines.

The dynamics of an electrical machine can be modelled accurately by time-stepping FEA. However, an electrical machine is always a part of a power transmission chain containing power electronics, control units, and mechanical parts. Although it is possible to combine a FE model to a system simulator [6], the requirements for the computational capacity limit the use of a comprehensive system model. Hence, simpler analytical models to depict the dynamics of electrical machines are needed.

The background of the study is based on the method applied by mechanical engineers. In me-

chanics, impulse response tests are used to identify vibration characteristics of mechanical structures. The structure is excited by an impulse and the response of the system is measured. Both excitation and response signals are converted to the frequency domain and from their ratio the frequency response function (FRF) is computed. A numerical method very similar to the mechanical impulse test has been successfully applied to identify electromagnetic force models [7].

In the paper, an analytical model for depicting small-signal behaviour of electromechanical torque with respect to torsional oscillations is presented. The analytical model is derived from the space-vector theory and the parameters of the model are estimated by using a numerical impulse response test [8], [9]. In the preceding work, the impulse has been applied to the stator voltage and the response of stator current has been studied. Here, the impulse is applied to the rotor position angle and the response of electromechanical torque is detected. This kind of model is considered useful since it can be combined with a mechanical torsion model to build a comprehensive electromechanical system model. The applicability of the voltage impulse test has been studied previously in [8]. In the presented paper, a similar study is performed for the angle impulse test.

The studied cage-induction machine has deep rotor bars. Thus, the influence of skin effect is studied and based on the results the small-signal model corresponding to a double-cage equivalent circuit is chosen. The circuit parameters obtained from the angle impulse test are compared with the parameters obtained from the voltage impulse test. In addition, the steady-state parameters are calculated using time-harmonic FEA [10]. Within the time-harmonic FEA, an effective permeability is applied and the obtained parameters are capable of depicting the rms-valued voltages and currents. These parameters are denoted by capital letters. The time-stepping FEA applies the instantaneous-value magnetization curve. The parameters obtained from the impulse tests are denoted by lower-case letters.

2 Methods

The work is based on numerical field computations and they are discussed first. Then, the analytical model of which the parameters are estimated using the FEA is presented. Next, the applicability of numerical impulse response test is studied. Lastly, the procedure for parameter estimation is presented.

2.1 Models

2.1.1 Finite-element models

The 2D finite-element model of an induction machine includes the magnetic saturation, skin effect in rotor bars, and rotation of rotor. Since the purpose of the study is to identify a suitable analytical model using the FEA, the differences between the analytical and FE model are one of the main objectives of the study. Distinguishing between different physical phenomena can be difficult in the case of complete FE model. However, the FE model can be simplified and brought closer to the analytical model.

The effect of saturation can be studied by modifying the material properties of FE model. In order to remove the effect of saturation, the saturable materials of cores and shaft are linearised. This means that the relative permeability is set to a constant value, for example 1000, instead of calculating it from the magnetisation curve. The results obtained from the linearised FE model are compared with the nonlinear FE model to evaluate the effect of saturation.

In the case of the cage-induction machine, the rotor bars are modelled as thick conductors when an eddy-current formulation is used [11]. Thus, the current density along the cross section depends on the rotor frequency. To remove the influence of the skin effect, the rotor of the cage-induction machine is replaced by a filamentary phase winding similar to slip-ring machines. When the supply voltage of the rotor is zero, the machine corresponds quite well to a cage-induction machine with uniform current density in the cross-sections of bars. If, in addition, the saturation is removed by linearizing the materials and the same operation point is computed, the differences between the computation results of the two FE models can be assumed to be mainly related to skin effect. The topic has been discussed more in [8]. The results obtained with the modified rotor are compared with the original cage rotor in Section 3.

2.1.2 Analytical model

The analytical model is derived from the space-vector theory. The skin effect can be included to the analytical model by adding another rotor branch to the circuit model. The double-cage circuit model is presented in Fig. 1.

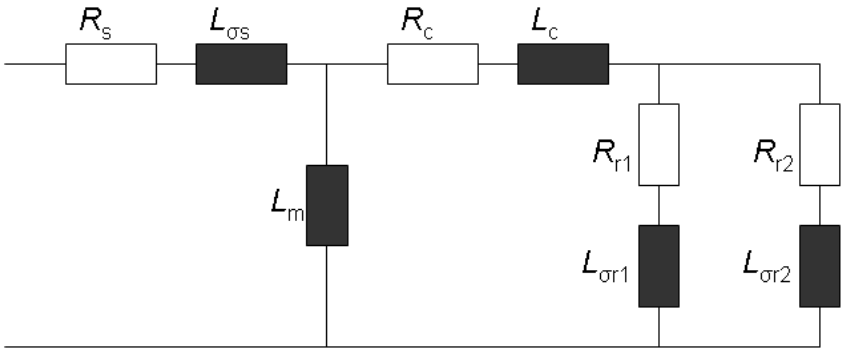

Fig. 1. A double-cage circuit model for induction machines.

The two parallel rotor branches consist of a resistance and leakage reactance. The rotor bars have common end-rings and their effect is modelled by the rotor resistance R_c and inductance L_c. In [12], the rotor branches are assumed to be equal in the way that both of the rotor currents flow through the mutual components L_c and R_c. This can be interpreted as if the cross-section of the rotor slot was divided into two sub-conductors. The voltage and flux linkage equations in the reference frame rotating at speed ω_k can be written as

$$\underline{u}_{\mathrm{s}}^{\mathrm{k}} = R_{\mathrm{s}}\underline{i}_{\mathrm{s}}^{\mathrm{k}} + \frac{\mathrm{d}\underline{\psi}_{\mathrm{s}}^{\mathrm{k}}}{\mathrm{dt}} + \mathrm{j}\omega_{\mathrm{k}}\underline{\psi}_{\mathrm{s}}^{\mathrm{k}} \tag{1}$$

$$0 = \left(R_{\mathrm{r1}} + R_{\mathrm{c}}\right)\underline{i}_{\mathrm{r1}}^{\mathrm{k}} + R_{\mathrm{c}}\underline{i}_{\mathrm{r2}}^{\mathrm{k}} + \frac{\mathrm{d}\underline{\psi}_{\mathrm{r1}}^{\mathrm{k}}}{\mathrm{dt}} + \mathrm{j}\left(\omega_{\mathrm{k}} - \frac{\mathrm{d}\theta_{\mathrm{r}}}{\mathrm{dt}}\right)\underline{\psi}_{\mathrm{r1}}^{\mathrm{k}} \tag{2}$$

$$0 = R_{\mathrm{c}}\underline{i}_{\mathrm{r1}}^{\mathrm{k}} + \left(R_{\mathrm{c}} + R_{\mathrm{r2}}\right)\underline{i}_{\mathrm{r2}}^{\mathrm{k}} + \frac{\mathrm{d}\underline{\psi}_{\mathrm{r2}}^{\mathrm{k}}}{\mathrm{dt}} + \mathrm{j}\left(\omega_{\mathrm{k}} - \frac{\mathrm{d}\theta_{\mathrm{r}}}{\mathrm{dt}}\right)\underline{\psi}_{\mathrm{r2}}^{\mathrm{k}} \tag{3}$$

$$\underline{\psi}_{\mathrm{s}}^{\mathrm{k}} = \left(L_{\mathrm{m}} + L_{\sigma\mathrm{s}}\right)\underline{i}_{\mathrm{s}}^{\mathrm{k}} + L_{\mathrm{m}}\left(\underline{i}_{\mathrm{r1}}^{\mathrm{k}} + \underline{i}_{\mathrm{r2}}^{\mathrm{k}}\right) \tag{4}$$

$$\underline{\psi}_{\mathrm{r1}}^{\mathrm{k}} = L_{\mathrm{m}}\underline{i}_{\mathrm{s}}^{\mathrm{k}} + \left(L_{\mathrm{m}} + L_{\mathrm{c}} + L_{\sigma\mathrm{r1}}\right)\underline{i}_{\mathrm{r1}}^{\mathrm{k}} + \left(L_{\mathrm{m}} + L_{\mathrm{c}}\right)\underline{i}_{\mathrm{r2}}^{\mathrm{k}} \tag{5}$$

$$\underline{\psi}_{\mathrm{r2}}^{\mathrm{k}} = L_{\mathrm{m}}\underline{i}_{\mathrm{s}}^{\mathrm{k}} + \left(L_{\mathrm{m}} + L_{\mathrm{c}}\right)\underline{i}_{\mathrm{r1}}^{\mathrm{k}} + \left(L_{\mathrm{m}} + L_{\mathrm{c}} + L_{\sigma\mathrm{r2}}\right)\underline{i}_{\mathrm{r2}}^{\mathrm{k}}. \tag{6}$$

Superscript *k* refers to the reference frame rotating with speed ω_{k}. θ_{r} is electrical rotor angle. Equation of motion is defined as

$$T_{\mathrm{L}} = -\frac{J}{p}\frac{\mathrm{d}\omega_{\mathrm{r}}}{\mathrm{dt}} + \frac{3}{2}pL_{\mathrm{m}}\,\mathrm{Im}\left\{\underline{\psi}_{\mathrm{s}}^{*}\underline{i}_{\mathrm{s}}\right\}. \tag{7}$$

If the currents are preferred as state-space variables, (4)-(6) are substituted to (1)-(3).

The small-signal model describes the dynamic behaviour of machine in the neighbourhood of some operation point. The small-signal model is derived applying small perturbations to the state-space variables. The equations are linearised by subtracting the steady-state quantities and neglecting the products of small perturbations [13]. The small-signal model is derived for the two-axis model obtained by separating (1)-(6) to real and imaginary parts and transforming to Laplace domain. Here, the voltages are assumed to be constant and all the voltage terms are cancelled. The initial values of perturbations are zero. In the synchronous reference frame, the steady-state current components are constants. The steady-state values are denoted by superscript 0. In the following, the superscript *k* is omitted for simplicity.

The current components can be solved as a function of rotor angle and substituted to the equation of torque to obtain the torque as a function of angle. First, separating the current terms and terms containing the perturbation of angle yields a matrix formulation

$$\begin{bmatrix} r_s+sl_s & -\omega_k^0 l_s & sl_m & -\omega_k^0 l_m & sl_m & -\omega_k^0 l_m \\ \omega_k^0 l_s & r_s+sl_s & \omega_k^0 l_m & sl_m & \omega_k^0 l_m & sl_m \\ sl_m & \left(\omega_r^0-\omega_k^0\right)l_m & r_c+r_{r1}+sl_{r1}^* & \left(\omega_r^0-\omega_k^0\right)l_{r1}^* & r_c+sl_c^* & \left(\omega_r^0-\omega_k^0\right)l_c^* \\ -\left(\omega_r^0-\omega_k^0\right)l_m & sl_m & -\left(\omega_r^0-\omega_k^0\right)l_{r1}^* & r_c+r_{r1}+sl_{r1}^* & -\left(\omega_r^0-\omega_k^0\right)l_c^* & r_c+sl_c^* \\ sl_m & \left(\omega_r^0-\omega_k^0\right)l_m & r_c+sl_c^* & \left(\omega_r^0-\omega_k^0\right)l_c^* & r_c+r_{r2}+sl_{r2}^* & \left(\omega_r^0-\omega_k^0\right)l_{r2}^* \\ -\left(\omega_r^0-\omega_k^0\right)l_m & sl_m & -\left(\omega_r^0-\omega_k^0\right)l_c^* & r_c+sl_c^* & -\left(\omega_r^0-\omega_k^0\right)l_{r2}^* & r_c+r_{r2}+sl_{r2}^* \end{bmatrix} \begin{bmatrix} \Delta i_{sx} \\ \Delta i_{sy} \\ \Delta i_{r1x} \\ \Delta i_{r1y} \\ \Delta i_{r2x} \\ \Delta i_{r2y} \end{bmatrix} \tag{8}$$

$$= -s\Delta\theta_r \begin{bmatrix} 0 \\ 0 \\ l_m i_{sy}^0 + l_{r1}^* i_{r1y}^0 + l_c^* i_{r2y}^0 \\ -l_m i_{sx}^0 - l_{r1}^* i_{r1x}^0 - l_c^* i_{r2x}^0 \\ l_m i_{sy}^0 + l_{r2}^* i_{r2y}^0 + l_c^* i_{r1y}^0 \\ -l_m i_{sx}^0 - l_{r2}^* i_{r2x}^0 - l_c^* i_{r1x}^0 \end{bmatrix}$$

The abbreviations are

$$\begin{aligned} l_s &= l_m + l_{\sigma s} \\ l_c^* &= l_m + l_c \\ l_{r1}^* &= l_m + l_c + l_{\sigma r1} \\ l_{r2}^* &= l_m + l_c + l_{\sigma r2} \end{aligned} \quad . \tag{9}$$

The small-signal electromagnetic torque is defined by

$$\Delta T_e = \frac{3}{2} p l_m \left[-\left(i_{r1y}^0 + i_{r2y}^0\right) \quad \left(i_{r1x}^0 + i_{r2x}^0\right) \quad i_{sy}^0 \quad -i_{sx}^0 \quad i_{sy}^0 \quad -i_{sx}^0 \right] \Delta \boldsymbol{i} , \tag{10}$$

where $\Delta \boldsymbol{i}$ is the current vector of (8). Dividing (8) and (10) with $\Delta\theta_r$ defines a new variable vector $\Delta \boldsymbol{i}/\Delta\theta_r$ and by applying it, the electromagnetic torque can be expressed as a function of rotor angle. Equations can be written in a short form as

$$\boldsymbol{A} \frac{\Delta \boldsymbol{i}}{\Delta \theta_r} = \boldsymbol{b} , \tag{11}$$

$$\frac{\Delta T_e}{\Delta \theta_r} = \boldsymbol{c} \frac{\Delta \boldsymbol{i}}{\Delta \theta_r} , \tag{12}$$

where $\boldsymbol{A}$ and $\boldsymbol{b}$ are obtained from (8) and $\boldsymbol{c}$ from (10). The electromagnetic torque as a function of rotor angle can be obtained by solving the current vector from (11), and substituting it to (12):

$$\frac{\Delta T_e}{\Delta \theta_r} = \boldsymbol{c}\boldsymbol{A}^{-1}\boldsymbol{b} \quad . \tag{13}$$

In frequency domain, Laplace variable s is replaced by $j\omega$. The symbolic solution of (13) is very long. Therefore, (13) is simplest to solve by substituting numerical values for the parameter estimates in (8) and calculating the FRF at each frequency separately. This approach is fast enough

to be implemented in curve-fitting algorithms.

2.2 Parameter estimation

2.2.1 Harmonic excitation

The term 'harmonic excitation' refers to a method in which a single excitation frequency component ω_d is added, for example, to the rotor angle. The purpose is to construct the FRF at one frequency at a time. Therefore, it is a very time-consuming method when using the time-stepping analysis. For a linear, time-invariant system, the response signals differ from zero only at the excitation frequency. In the case of a nonlinear or time-variant system, the response signal excited at one frequency may contain other frequencies. In the time-stepping FEA, such physical effects as saturation of iron and rotation of a slotted rotor are modelled. These effects are included in the space-vector theory. However, if the amplitudes of the excess components are very small compared to the excited frequency, their effect can be neglected. Here, the response of the electromagnetic torque is assumed to behave linearly with respect to small speed oscillations around a constant speed operation. As far as the frequencies do not interfere with each other, it is possible to excite several frequencies simultaneously.

2.2.2 Impulse response test

The purpose of impulse test is to produce FRF corresponding to the one obtained from the harmonic excitation but with smaller number of computations. The impulse excitation is applied to the rotor position angle. The geometrical angle is denoted by Θ_r as a distinction to electrical angle θ_r. The shape of the impulse depends on time according to

$$\Delta\Theta_r(t) = \begin{cases} a_{rel}\tau_p \sin(2\pi f_d t), & t_1 \le t \le t_1 + t_d \\ 0, & \text{otherwise} \end{cases}, \tag{14}$$

where the amplitude is defined by the relative amplitude a_{rel} and the pole pitch τ_p. t_1 is the time instant at the beginning of the impulse and t_d the duration time. f_d is chosen so that the shape of the impulse is a half of a sine wave. The impulse is presented in Fig. 2. The amplitude is exaggerated for visualisation purposes.

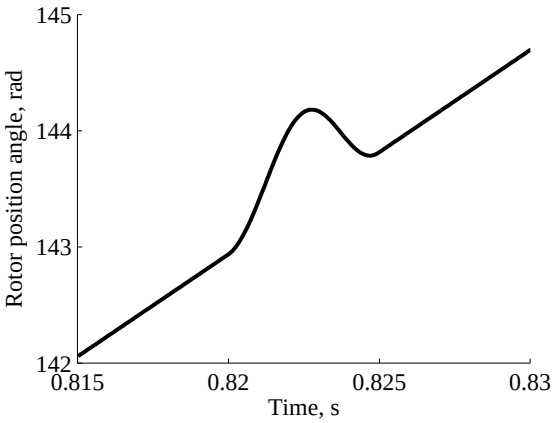

Fig. 2. Impulse excitation applied to the rotor angle.

The impulse should excite all the frequencies in the frequency range studied. The length of the impulse defines the frequency contents obtained. For example, an impulse of length 10 ms has a nonzero frequency contents up to 200 Hz [14]. By shortening the impulse, a wider frequency contents can be obtained. By using an impulse length of 1 ms, a frequency range up to 2000 Hz has been studied. However, it is detected that the range of 0…100 Hz contains the important dynamics in the scope of this study.

The machine is simulated until the response of the torque has completely decayed and the machine has returned to the steady-state. Typically, 20 000 time-steps providing a frequency resolution of 1 Hz are sufficient. The electrical machine produces certain frequencies within its normal operation. In order to distinguish the impulse response, the steady state has to be cancelled. This is performed by computing the same operation point without any impulse excitation and subtracting the computation results from the perturbed case. The impulse to the angle, $\Delta\theta_\mathrm{r}$, and the response of the electromagnetic torque, ΔT_e, are converted to the frequency domain using DFT. From their ratio, the FRF of the electromagnetic torque is obtained. Since the rotor angle and torque are real-valued signals, the FRF in the negative frequency region is the complex conjugate of the positive region and can be omitted.

The small-signal parameters are obtained from the curve fitting performed using Differential Evolution [15]. In the estimation, the sum of squared differences between real and imaginary parts of computed FRF and the FRF obtained from (13) is minimised. In the case of the impulse test, the frequency range used for estimation is 0…90 Hz with a resolution of 1 Hz. For every set of parameter estimates, (13) is solved at each frequency and the result is compared with the computed FRF. The minimum is reached in at most 2000 iterations.

3 Results

An 850 kW cage-induction machine is studied. The finite-element mesh consists of 4136 triangular second-order elements and 4136 nodes. The cross-section of a rotor bar is shown in Fig. 3 and the rated values are given in Table 1. In Fig. 3, also the division of the rotor bar into two sub-

conductors is shown. The division follows the element edges and it is used in the estimation of steady-state parameters [10].

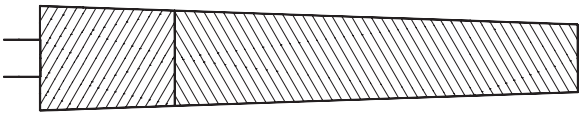

Fig. 3. Cross-section of rotor bar. The height of the bar is 55 mm.

Table 1. Rated values of the cage-induction machine studied.

P_N [kW]	rated power	850
U_{sN} [V]	rated stator voltage	690 (delta)
p	number of pole pairs	3
f_N [Hz]	rated stator frequency	50
s_N [%]	rated slip	0.53

3.1 Study of applicability of the impulse test

First, the applicability of the impulse response test is studied. The harmonic excitation with the relative amplitude a_{rel} of 1 % for the sine wave is performed at 23 frequencies and the FRF is calculated at each frequency point. The results are compared with the FRF obtained by an impulse test with a_{rel} = 1 %. The comparison is presented in Fig. 4.

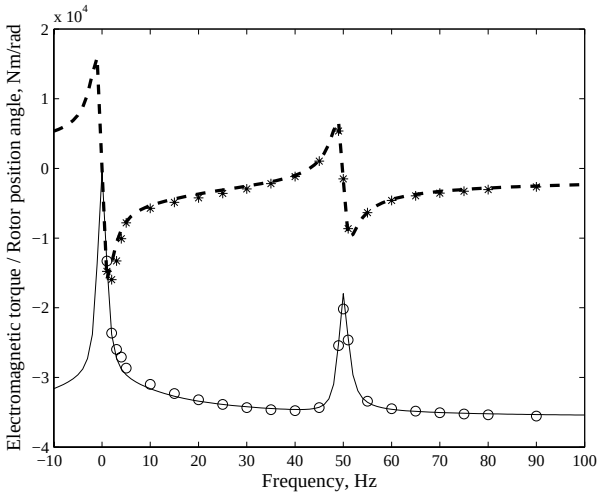

Fig. 4. Comparison between the FRFs obtained from the impulse test (real part solid, imag. part dashed), and harmonic excitation (real o, imag. *).

First of all, it can be noted that both the impulse test and harmonic excitation depict a frequency range where the imaginary parts of FRFs are positive. If an FRF is defined between the angular speed and torque, the real part defines whether the electromagnetic damping of the machine is positive or negative [16]. However, when the rotor angle acts as an excitation signal, the corre-

sponding damping factor is the imaginary part so that when it is positive the damping is negative. This indicates a possibility to torsional oscillations and instability. The topic is studied more in Section 3.3.

In general, the FRFs coincide well. The difference for the real part is less than 2 % and imaginary part less than 12 %. However, at 50 Hz the real parts differ notably. The supply frequency is 50 Hz and when a small 50 Hz perturbation is added to the rotor angle, some interaction, for example power transfer, may occur. Also at 3 and 4 Hz, the differences between the imaginary parts are more prominent, around 20 %. The similar computations are performed using a_{rel} = 10 % for the impulse test and the harmonic excitation. The differences between the obtained FRFs are of the same magnitude as with a_{rel} = 1 %.

The effect of the amplitude is studied performing the impulse test with a_{rel} = 1…50 %. The tests are performed at the rated load using the same initial steady state. Fig. 5 shows the comparison between a_{rel} of 1, 5 and 10 %. The differences between the FRFs obtained with a_{rel} of 1 and 10 % are 2…5 %. At the frequencies higher than 70 Hz, the difference between imaginary parts begins to increase. Around 50 Hz, the differences are also a little larger. With a_{rel} = 20 %, the shape of the FRF begins to change more visibly and with a_{rel} = 50 % the FRF is clearly distorted.

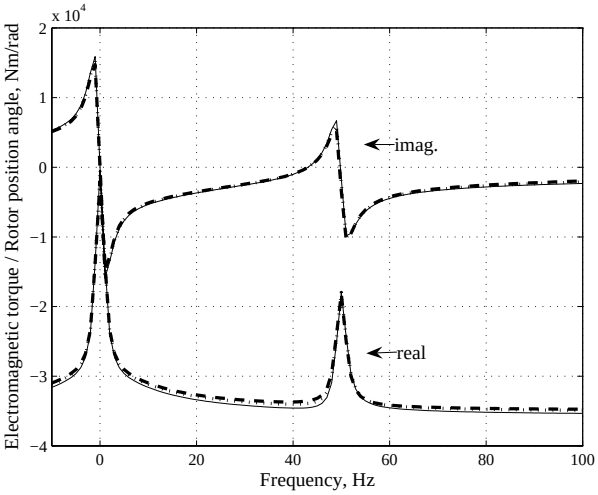

Fig 5. FRFs at relative amplitudes of 1 % (solid) , 5 % (dotted) and 10 % (dashed).

The influence of skin effect in the rotor bars is studied in order to evaluate the order needed for the circuit model. The cage rotor of the FE model is replaced by a three-phase winding with thin conductors in which the current density is constant. The winding is chosen so that the FE model corresponds to the original FE model. The saturable materials of the FE models are linearised by setting a constant permeability. The comparison between the FRFs obtained using the two linearised FE models is presented in Fig. 6. Fig. 6 shows that the skin effect has a significant influence on the FRF. It is concluded that a double-cage small-signal model is more suitable for the parameter estimation.

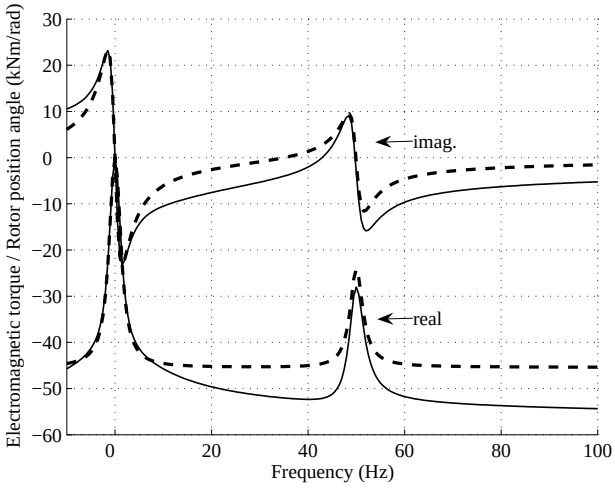

Fig 6. Comparison between the linearised FE models: skin effect included (solid line), skin effect removed (dashed line).

3.2 Parameter estimation

First, the steady-state parameters for a double-cage circuit model are estimated using the impedance method. The parameters are estimated using the data from both the nonlinear and linearised FE models. The results are presented in Table 2.

Table 2. Parameters obtained from the impedance method.

		Impedance method	
		Linear	Nonlin.
R_s	[mΩ]	2.840	2.840
$L_{\sigma s}$	[mH]	0.1387	0.2771
L_m	[mH]	4.294	5.983
L_c	[mH]	0.1165	0.1188
R_c	[mΩ]	0.7362	0.7338
$L_{\sigma r1}$	[mH]	–0.00812	–0.00713
R_{r1}	[mΩ]	5.916	5.907
$L_{\sigma r2}$	[mH]	0.07996	0.08028
R_{r2}	[mΩ]	2.426	2.418

The estimated $L_{\sigma r1}$ is negative. This is associated with the reference of rotor variables to the stator. For the two sub-conductors, separate reference factors are computed in order to obtain a more accurate estimate for the electromagnetic torque [10]. On the other hand, the leakage of the upper sub-conductor is very small. After the reference to the stator, the self reactance can become slightly smaller than the mutual reactance producing a negative leakage reactance. This phenomenon occurs at high loads. If the same reference factor is used for both rotor cages all the parameter estimates are positive.

The double-cage model contains nine physically reasonable parameters. Some restrictions can be made to simplify the estimation. The stator resistance is assumed to be known but it could be estimated as well. The mutual rotor resistance depicting the effect of end-rings is assumed to be equal to the one given by the impedance method. It could also be neglected from the small-signal model without reducing the goodness of the fit. In that case, its effect is lumped to the other rotor parameters which are slightly changed. It can be seen from (2)–(3) and (5)–(6) that the rotor equations are equivalent by structure and the order can be changed arbitrarily. Therefore, there exist at least two sets of parameters which can provide an equally good fit. The possibility for obtaining several minima can be avoided by modifying the rotor equations to be different. The easiest way is to assign another leakage inductance to be zero. Moreover, the leakage between the stator and rotor cannot be obtained from the stator quantities only. Thus, the ratio between the stator and rotor leakage reactance is fixed to the value given by the impedance method. This ratio could be obtained by some other method as well. When the remaining five parameters are estimated and l_{r2} is calculated, the estimation procedure gives the same parameter set every time. However, neglecting the other leakage reactance has a small impact on the values of parameter estimates. This should be considered when comparing the parameters estimated with different methods.

The small-signal model contains steady-state current components $\boldsymbol{i}_s^0$ and $\boldsymbol{i}_r^0$ (vectors). It has been noticed that when using the presented model in the estimation, all the rotor current components cannot be estimated. The components of stator current are obtained from the steady-state time-stepping analysis. The rotor current components can be calculated by current division using the known stator current and the steady-state circuit model (Fig. 1 and Table 2). However, since the steady-state parameters are obtained from another estimation method, they do not necessarily suite the small-signal model best. Another alternative is to fix the total rotor current to some reasonable value and estimate the current components of one branch while calculating the components of another branch from the total rotor current. It is observed that the latter option gives a slightly better fit. The current components are presented in Table 3. For the nonlinear FE model, both fixed and partly estimated current components are tried in estimation.

Table 3. Steady-state current components.

		Linear $\boldsymbol{i}_r^0$ fixed	Nonlin. $\boldsymbol{i}_r^0$ fixed	Nonlin. $\boldsymbol{i}_{r1}^0$est.
i_{sa}^0	[A]	1091.90	1020.80	1020.80
i_{sb}^0	[A]	-623.76	-565.91	-565.91
i_{r1a}^0	[A]	-673.53	-313.11	641.75
i_{r1b}^0	[A]	116.24	73.43	1.99
i_{r2a}^0	[A]	-453.41	-752.29	-1707.15
i_{r2b}^0	[A]	99.71	222.54	293.97
i_{ra}^0	[A]	-1126.94	-1065.40	-1065.40
i_{rb}^0	[A]	215.95	295.97	295.97

The parameters are estimated using both the angle impulse test and the voltage impulse test [9]. They are estimated for both the linearised and nonlinear FE models. In order to compare the effect of steady-state current components, both sets from Table 3 are tried. The parameter estimates are presented in Table 4. The fixed parameters are denoted with asterisk and the calculated leakage reactance with two asterisks.

Table 4. Parameters obtained from the voltage and angle impulse tests.

		Linear iron in the FE model		Nonlinear iron in the FE model		
		voltage imp.	angle imp. $\boldsymbol{i}_r^0$ fixed	voltage imp.	angle imp. A $\boldsymbol{i}_r^0$ fixed	angle imp. B $\boldsymbol{i}_{r1}^0$est.
r_s	[mΩ]	2.84*	2.84*	2.84*	2.84*	2.84*
$l_{\sigma s}$	[mH]	0.06172	0.08702	0.1204	0.1426	0.1441
l_m	[mH]	2.722	4.1893	3.917	6.1092	6.1485
l_c	[mH]	0.1855	0.1387	0.2557	0.2058	0.2087
r_c	[mΩ]	0.7372*	0.7372*	0.7344*	0.7344*	0.7344*
$l_{\sigma r1}$	[mH]	0*	0*	0*	0*	0*
r_{r1}	[mΩ]	9.277	9.5557	9.346	7.414	7.5458
$l_{\sigma r2}$	[mH]	0.06942**	0.04981**	0.06893**	0.08161**	0.08248**
r_{r2}	[mΩ]	2.938	2.4396	2.745	2.4258	2.4201

In all the cases, the fits are good and the differences between the data and the estimate are within few percents. The best fit, less than 1 % of difference, is obtained using the voltage impulse test for the nonlinear FE model.

The most practical formulation for the small-signal model is a transfer function. It is obtained by substituting the parameters to (8)–(9) and solving (13). For the nonlinear FE model with the parameters obtained from the angle impulse test (Table 4), the transfer function

$$\frac{\Delta T_{\mathrm{e}}(s)}{\Delta \theta_{\mathrm{r}}(s)} = \frac{-3.58\cdot 10^{4} s^{6} - 9.765\cdot 10^{6} s^{5} - 4.256\cdot 10^{9} s^{4} - 9.417\cdot 10^{11} s^{3} - 6.405\cdot 10^{13} s^{2} - 3.47\cdot 10^{14} s}{s^{6} + 305.4\, s^{5} + 1.258\cdot 10^{5} s^{4} + 2.911\cdot 10^{7} s^{3} + 2.241\cdot 10^{9} s^{2} + 2.54\cdot 10^{10} s + 8.378\cdot 10^{10}} \tag{15}$$

is obtained. When the roots of the numerator and denominator of (15) are solved, the poles and zeros of the transfer function can be studied. For comparison, the transfer functions obtained by using the parameters from the harmonic excitation and the impedance method are also calculated. The zeros and poles are presented in Table 5. At the DC, the output is zero indicating that if the rotor angle is shifted by some constant, the electromagnetic torque is not affected.

Table 5. Zeros and poles obtained from the harmonic excitation and impedance method.

Angle impulse test		Impedance method	
zeros	poles	zeros	poles
0	–6.42 ± 1.80i	0	–4.91 ± 1.76i
–4.17 ± 313.87i	–8.05 ± 313.64i	–3.75 ± 313.96i	–7.02 ± 313.81i
–5.9188	–138.25 ± 2.05i	–4.4361	–151.83 ± 1.91i
–119.95		–137.27	
–138.57		–151.64	

In addition to model (13), the frequency response data can be fitted to a transfer function in which the order of the numerator and denominator are chosen and coefficients are estimated. The method has been presented in [17] and it is available in Matlab®. By trying with different orders, it is noticed, that the numerator and denominator have to be of the same order in order to get a reasonable fit. The fourth, fifth and sixth order transfer functions give a good fit. As a distinction to (13) and (15), the transfer functions obtained by this method always contain a zero-order term in the numerator. However, in the transfer functions, one zero is close to zero. The sixth order model corresponds best to (15) by its structure. However, in the estimated transfer function a zero and a pole are very close to each other and the numerical inaccuracies may cause problems. The fourth order model

$$\frac{\Delta T_{\mathrm{e}}(s)}{\Delta \theta_{\mathrm{r}}(s)} = \frac{(s+0.43499)\left[s-(-4.2394+313.44\mathrm{i})\right]\left[s-(-4.2394-313.44\mathrm{i})\right](s+118.49)}{(s+7.4087)\left[s-(-7.9582+313.66\mathrm{i})\right]\left[s-(-7.9582-313.66\mathrm{i})\right](s+135.01)} \tag{16}$$

appears to be the best choice for an alternative for (15) since the poles are close to the ones in (15). From the poles of (15) and (16), it can be seen that the electromagnetic system itself is stable. However, when the electrical machine is connected to another system, it can exchange energy and such properties as damping become significant. The topic is discussed next.

3.3 Study and measurements with 37-kW machines

In Section 3.1, it was noted that there exists a frequency range of negative damping and therefore a possibility to oscillation and instabilities within the computed FRFs. In order to study the effect of the predicted negative damping, measurements are performed using two almost identical 37-kW cage-induction machines. The rated voltage of the machines is 380 V, rated slip 2.0 %, and rated current 71 A.

First, a similar numerical impulse test as for the 850-kW machine has been performed at several operation points. In the case of synchronous machines, the effect of stator resistance on damping has been studied analytically, for example, in [16]. It is concluded that with $r_s = 0$ the damping is always positive. Increasing the stator resistance, however, widens the range of negative damping. The measured resistance of the supply cables is 53 % of the stator resistance and it is included in the total stator resistance, 121 mΩ, of the FE model. For comparison, the impulse test is also performed at no-load condition but neglecting the stator resistance. The FRF computed with $r_s = 121$ mΩ is presented in Fig. 7(a) and the FRF obtained with $r_s = 0$ is presented in Fig. 7(b). The rotor position angle is presented in electrical degrees.

At $r_s = 0$, the negative damping disappears. At the measured r_s, the negative damping occurs at the frequency range of 36.5…46.5 at no-load condition. Based on the computations at different loads, it is noted that increasing the load widens the frequency range and increases the magnitude of negative damping. However, no-load operation is chosen as it can be studied with a relatively simple measurement set-up. The machines are coupled with a thin, long shaft designed so that the effects of mechanical damping are minimised. The natural frequency of the purely mechanical system is designed to 36 Hz. The supply frequency of the machines is adjusted to bring the frequency range of the predicted negative damping close to the mechanical natural frequency. The machines are supplied from a 750-kVA synchronous generator. The flux is kept constant by adjusting the supply voltage along with the frequency. The measurement set-up is shown in Fig. 8.

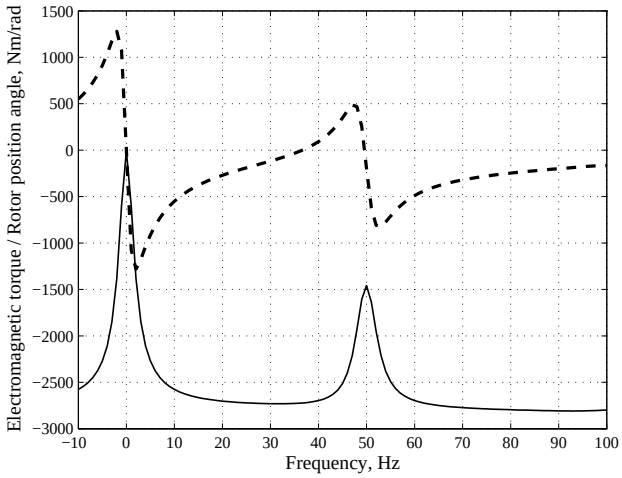

(a)

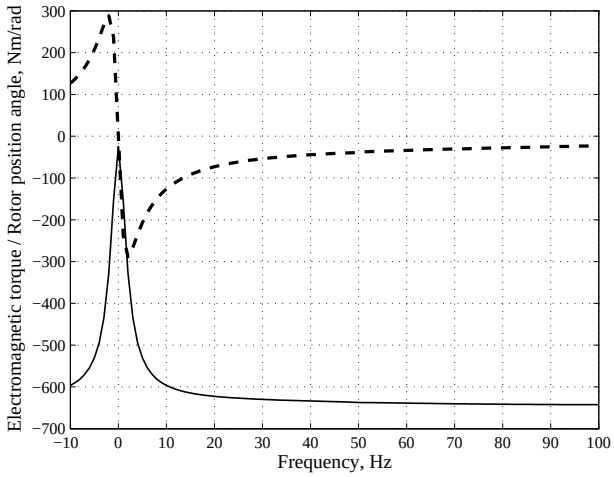

(b)

Fig 7. Computed FRF of the 37-kW cage-induction machine at no load, (a) r_s = 121 mΩ and (b) r_s = 0.

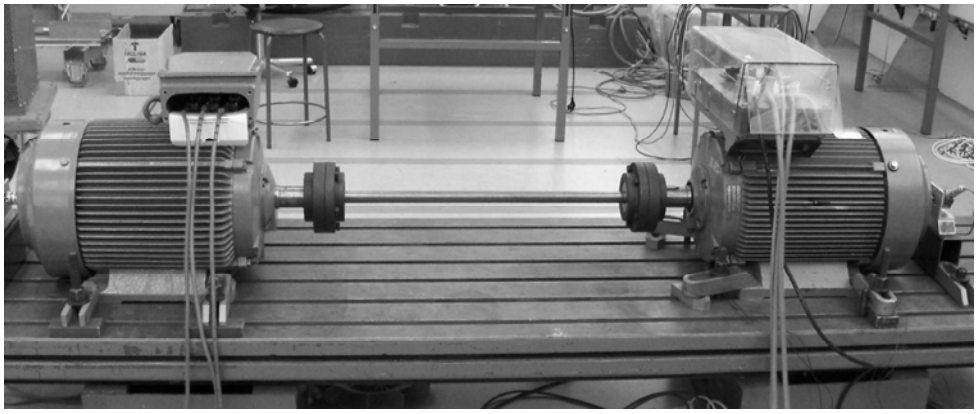

Fig 8. The measurement set-up.

Pulse tachometers are used to detect the torsional oscillations. At the same time, the stator currents are measured since the harmonics related to oscillations can be observed at frequencies $f = f_s \pm \Delta f_r$ [18], where Δf_r is the frequency of torsional oscillations. The frequency resolution is 0.125 Hz. Torsional oscillations are detected at the supply frequencies of 40…52 Hz. Fig. 9(a) shows the amplitude of torsional oscillations as a function of the supply frequency and Fig. 9(b) the corresponding amplitudes of current harmonic $f_s + \Delta f_r$ normalised with respect to the fundamental no-load current. The magnetic field of the machine acts as an additional torsional spring stiffening the torsional system. The real part of the FRF represents the additional spring constant. Thus, the oscillation frequency increases as well from the purely mechanical 36 Hz to 39.25…39.75 Hz. It increases slightly along with the supply frequency.

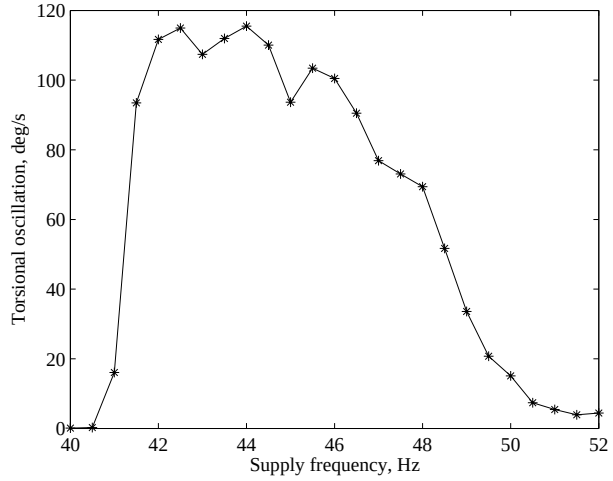

(a)

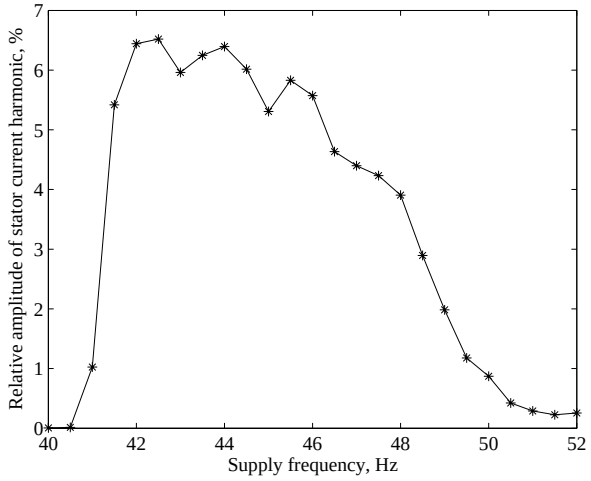

(b)

Fig 9. (a) Torsional oscillations as a function of supply frequency, (b) induced current harmonic $f_s + \Delta f_r$.

4 Discussion

The comparison between the FRFs obtained from the impulse test and the harmonic excitation show a good agreement. To maintain the linearity, the relative amplitude of the impulse has to be less than 20 % of the pole pitch. Within the study, three different sets of parameters were obtained. Based on the previous study [9], the parameters given by the impedance method are suitable for depicting the steady state whereas the parameters obtained from the voltage impulse test are able to model small-signal behaviour. Whether the effective or incremental permeability is applied in the FEA can be seen especially from the values of magnetising inductances. This can be observed from Table 4 as well. However, the parameters obtained from the angle impulse test are closer to the steady-state parameters. In [19], it was concluded that the incremental changes affecting the amplitude of the magnetising flux are related to the incremental permeability whereas the changes affecting the phase are related to the effective permeability. The results of the angle impulse test coincide with the concept.

In Section 3.3, it was noted that if the stator resistance is neglected, the range of the negative damping disappears. The effect of the stator resistance is studied more closely by simulations for the 850-kW machine. When the impulse test is performed with a half of the original stator resistance, the range of negative damping is reduced from 43…50 Hz to 46…50 Hz. When neglecting the stator resistance, the negative damping is removed as well as in the case of 37-kW machine (Fig.7 (b)). With the small-signal model, the effect of stator resistance can be studied by fixing the other parameter estimates and calculating the transfer function (13) when the value of r_s is gradually decreased. It can be noticed that decreasing r_s increases the real part of the first pole (Table 5) linearly and at r_s=0 the real part of the pole is practically zero as well. On the other hand, the other poles are almost unaffected by the value of stator resistance.

The existence of negative damping is related to the stator current harmonics induced by torsional oscillation. The physical phenomenon has been depicted also in [1] by using hunting-frequency networks. When the rotor oscillates in the main flux, the induced electromotive force produces current harmonics which are coupled to the stator (Fig. 9). When the oscillation frequency approaches the supply frequency, the lower stator current harmonic approaches dc in the stator reference frame. At low frequencies, the stator resistance is dominant over the reactance and defines the phase and amplitude of the current harmonic. Because of the strong coupling the rotor current harmonic changes accordingly. The phase of the upper stator current harmonic, however, is dominated by the reactances within the whole frequency range studied. The sign of the damping depends on the balance of the harmonic torque components. Within a relatively narrow frequency range the harmonic torque can have such a phase that it supplies power to the oscillation. In a special case where $r_s = 0$, the reactance dominates and defines the phase. The damping remains positive.

The frequency range of the measured oscillations coincides well with the range of the negative damping predicted by the impulse test. However, the amplitude of measured oscillations is lim-

ited to relatively small values and a full instability does not occur. A mechanical model corresponding fairly well to the measurement set-up is combined to a FE model of a single machine. It can be assumed that the middle point of the shaft rotates at a constant speed since the oscillations of the two machines are of equal amplitudes but opposite phases with respect of that point. Thus, the middle point can be treated as a large mass of inertia. When operation points corresponding to the measurements are computed, it is noted that the resulting oscillations are limited as well. The nonlinearities of the system limit the oscillation amplitude and prevent the instability. However, the computed amplitudes would be high enough to break the shaft. The significant difference between the results of the FEA and the measurements can be related to mechanical damping or such electromagnetic losses which are not modelled by the 2D time-stepping FEA. The nonlinear damping observed will be an objective of a future study. Moreover, the FRF of the 37-kW machine will be defined by measurements.

5 Conclusions

A small-signal model for predicting the torsional oscillations of a deep-bar 850-kW cage-induction machine is presented. The estimation data to obtain the model parameters are provided by the time-stepping FEA. The analytical model can be fitted well to the numerical data and the obtained parameters are physically reasonable. The impulse test depicts a frequency range of negative electromagnetic damping. This indicates oscillations when the machine is connected to a mechanical system. The phenomenon is studied by measurements using two 37-kW cage-induction machines. Torsional oscillations are detected at those supply frequencies for which the numerical impulse response test predicts negative damping.

References

[1] Concordia, C.: “Induction motor damping and synchronizing torques”, AIEE Transactions Power Apparatus and Systems, Vol. 71, January 1952, pp. 364–366.

[2] Valenzuela, M.A., Bentley, J.M.: “Dynamic compensation of torsional oscillation in paper machine sections”, IEEE Trans. Ind. App., Vol. 41, No. 6, November/December 2005, pp. 1458–1466.

[3] Nelson, R.H., Lipo, T.A., Krause, P.C.: ”Stability Analysis of a Symmetrical Induction Machine”, IEEE Trans. PAS, Vol. PAS-88, No. 11, November 1969, pp. 1710–1717.

[4] IEEE Torsional Issues Working Group, “Fourth supplement to a bibliography for study of subsynchronous resonance between rotating machines and power systems”, IEEE Trans. Power Syst., Vol. PWRS-12, August 1997, pp. 1276–1282.

[5] Tabesh, A., Iravani, R.: “Frequency-response analysis of torsional dynamics”, IEEE Trans. Power Syst., Vol. 19, No. 3, August 2004, pp. 1430–1437.

[6] Kanerva, S., Seman, S., Arkkio, A.: ”Inductance Model for Coupling Finite Element Analysis with Circuit Simulation”, IEEE Trans. Magn., Vol. 41, No. 5, May 2005, pp. 1620–1623.

[7] Holopainen, T.P.: “Electromechanical interaction in rotor dynamics of cage induction motors”, Doctoral Thesis, Helsinki University of Technology, 2004.

[8] Repo, A.-K., Arkkio, A.: ” Numerical impulse response test to estimate circuit-model parameters for induction machines”, IEE Proc – EPA, Vol. 153, No. 6, November 2006, pp. 883–890.

[9] Repo, A.-K., Arkkio, A.: ” Numerical impulse response test to identify parametric models for closed-slot deep-bar induction motors”, IET Proc – EPA, Vol. 1, No. 3, May 2007, pp. 307–315.

[10] Repo, A.-K., Niemenmaa, A., Arkkio, A.: ”Estimating circuit models for a deep-bar induction motor using time harmonic finite element analysis”, Proc. Int. Conf. Electrical Machines, Crete, Creece, 2006, [IEEE], on CD No. 614.

[11] Arkkio, A.: “Analysis of Induction Motors Based on the Numerical Solution of the Magnetic Field and Circuit Equations”, Electrical Engineering Series, No. 59, Acta Polytechnica Scandinavica, Helsinki 1987, 97 p., available: http://lib.tkk.fi/Diss/198X/isbn951226076X/.

[12] Levi, E.: “Main Flux Saturation Modelling in Double-Cage and Deep-Bar Induction Machines”, IEEE Trans. Ener. Conv., Vol. 11, No. 2, June 1996, pp. 305–311.

[13] Krause, P.C., Wasynczuk, O., Sudhoff, S.D.: “Analysis of Electric Machinery and Drive Systems”, (John Wiley & Sons, 2002 2nd edn).

[14] Ewins, D.J.:”Modal testing: theory, practice and application”, 2nd edition, Research studies press Ltd., Hertforshire, England, 2000.

[15] Price, K.V., Storn, R.M., Lampinen, J.A.: “Differential evolution: a practical approach to global optimization”, Springer Berlin, 2005.

[16] Kovacs, P.K.: “Transient Phenomena in Electrical Machines”, Elsevier, 1984.

[17] Levi, E.C.: "Complex-Curve Fitting", IRE Trans. Automatic Control, Vol. AC-4, 1959, pp.37–44.

[18] Canay, M: “Subsynchronous resonance – an explanation of the physical relationships”, Brown Boveri Review, Vol. 68, No. 8/9, August/September 1981, pp. 348–357.

[19] Melkebeek, J.A.A., Novotny, D.W.: “The Influence of Saturation on Induction Machine Drive Dynamics”, IEEE Trans. Ind. Appl., Vol. IA-19, No. 5, September/October 1983, pp. 671–681.